3-D inviscid self-excited vibrations of a blade row in the last stage turbine

R. Rządkowski[a,*], V. Gnesin[b]

[a]Institute of Fluid-Flow Machinery, Polish Academy of Sciences, Fiszera 14, PL 80-952 Gdańsk, Poland
[b]Institute for Problems in Machinery, Ukrainian National Academy of Sciences, 2/10 Pozharsky Street, Kharkov 310046, Ukraine

Abstract

Presented here is a three-dimensional (3-D) nonlinear time-marching method for the aeroelastic behaviour of an oscillating turbine blade row. The approach has been based in the solution of a coupled fluid–structure problem where the aerodynamic and structural dynamic equations are integrated simultaneously in time. This provides the correct formulation of a coupled problem, as the interblade phase angle (IBPA) at which stability (instability) would occur is also a part of solution. The ideal gas flow around multiple interblade passages (with periodicity in the entire annulus) is described by the unsteady Euler equations in conservative form, which are integrated by using the explicit monotonic second-order accurate Godunov–Kolgan finite-volume scheme and a moving hybrid H–O (or H–H) grid. The fluid and the structural equations are solved using the modal superposition method. An aeroelasticity prediction of a turbine blade of 0.765 m is presented. The natural frequencies and modal shapes of the blade were calculated by using 3-D finite element models. The instability regions for five mode shapes and the distribution of the aerodamping coefficient along the blade length were shown for harmonic oscillations with an assumed IBPA. The coupled fluid–structure oscillations in which the IBPA is part of the solution are shown.
© 2007 Elsevier Ltd. All rights reserved.

Keywords: Blades; Flutter; Inviscid flow

1. Introduction

Aeroelasticity analyses of turbomachinery blades require the study of a fluid–structure system exposed to unsteady dynamic loading. The nature of the flow in turbomachines is complicated due to the co-existence of subsonic, supersonic and transonic regions. Blade vibration and its interaction with the fluid flow add another dimension to the problem.

A literature survey on flutter prediction methods is beyond the scope of this paper and the interested reader should consult Marshall and Imregun (1996). However, a brief overview will be given here for the sake of completeness.

Most flutter computations consider a typical sector vibrating in a given assembly mode (or interblade phase angle (IBPA)) for which flutter is expected to occur. In such a usually linear analysis, the IBPA must be prescribed at the periodic boundaries.

*Corresponding author.

E-mail address: z3@imp.gda.pl (R. Rządkowski).

Nomenclaute		t	$\tau/316$ time (s)
		δ	interblade phase angle (deg.)
IBPA	interblade phase angle (deg.)	ε	internal energy of mass unit
H	source vector	χ	ratio of the fluid specific heats
p	pressure (MPa)		

New approaches have been developed based on the simultaneous integration in time of the equations of motion for the structure and fluid (Bakhle et al., 1992; He, 1984; Moyroud et al., 1996; Rządkowski et al., 1998; He and Ning, 1998; Bendiksen, 1998; Gnesin and Kolodyazhnaya, 1999; Gnesin et al., 2001; Carstens and Belz, 2000; Gnesin et al., 2000). These approaches are very attractive due to the correct formulation of a coupled problem, as the IBPA at which stability (instability) would occur is part of the solution. In the above papers the considered blades were untwisted and short with nonvariable nonsymmetrical cross-sectional areas along the blade length.

In this paper, a twisted blade of $L = 0.765$ m length with variable cross-sectional area along the blade length was considered in the flutter calculation. For each mode in turn the individual stability and aerodynamic coefficient along the blade length is shown.

2. Aerodynamic model

Here the three-dimensional (3-D) transonic flow of an ideal gas through a multipassage blade row is considered. In most cases the flow is assumed to be an aperiodic function from blade to blade (in a pitchwise direction), so the calculated domain includes all blades of the entire assembly.

The flow equations are written for a three-dimensional Cartesian coordinate system, which is fixed to a rotating blade row. In this case, the conservative form of the unsteady Euler equations is given by

$$\frac{\partial}{\partial t} \int_{\Omega} f \, d\Omega + \oint_{\sigma} \vec{F} \cdot \vec{n} \, d\sigma + \int_{\Omega} H \, d\Omega = 0, \tag{1}$$

where f is the solution vector, $\vec{F}$ the inviscid flux through the lateral area σ bounding the finite volume Ω, and H is the source vector, which contains the terms due to the rotation of the coordinate system. These components can be written as (Gnesin and Rządkowski, 2000)

$$f = \begin{bmatrix} \rho \\ \rho v_1 \\ \rho v_2 \\ \rho v_3 \\ E \end{bmatrix}, \quad \vec{F} = \begin{bmatrix} \rho \vec{v} \\ \rho v_1 \vec{v} + \delta_{1i} p \\ \rho v_2 \vec{v} + \delta_{2i} p \\ \rho v_3 \vec{v} + \delta_{3i} p \\ (E+p)\vec{v} \end{bmatrix}, \quad H = \begin{bmatrix} 0 \\ \rho a_{e1} - 2\rho\omega v_2 \\ \rho a_{e2} + 2\rho\omega v_1 \\ 0 \\ 0 \end{bmatrix}, \quad \delta_{ji} = \begin{cases} 1, & j=i, \\ 0, & j \neq i, \end{cases}$$

where p and ρ are the pressure and density, v_1, v_2, v_3 are the velocity components, a_{e1} and a_{e2} are the transfer acceleration projections, ω is the rotational angular velocity,

$$E = \rho\left(\varepsilon + \frac{v_1^2 + v_2^2 + v_3^2 - r^2\omega^2}{2}\right),$$

is the total energy of volume unit, r is the distance from rotation axis, and ε is an internal energy per mass unit.

The above system of equations is completed by the perfect gas equation

$$p = \rho\varepsilon(\chi - 1), \tag{2}$$

where χ denotes the ratio of the fluid specific heats. The spatial solution domain is discretized using linear hexahedral elements. Eqs. (1) and (2) are integrated on a moving H–H (H–O)-type grid with the use of the explicit monotonic second-order accuracy Godunov–Kolgan difference scheme (Gnesin and Rządkowski, 2000).

In the Godunov method the numerical fluxes are obtained from the solution of the Riemann problem in a normal direction (unit normal $\vec{n}^0$) to the elementary cell surface. The position of the normal is defined by three direction cosines of angles (α, β, γ), between the normal and coordinate axes. It is obvious that the following relation holds:

$$|\vec{n}^0| = \alpha^2 + \beta^2 + \gamma^2 = 1.$$

Let $\vec{n}_1^0 = \{\alpha_1, \beta_1, \gamma_1\}$, $\vec{n}_2^0 = \{\alpha_2, \beta_2, \gamma_2\}$, $\vec{n}_3^0 = \{\alpha_3, \beta_3, \gamma_3\}$ be external normals to the cell surfaces, which are perpendicular to the axes x, y and z, respectively. Then the symbolic vector of fluxes, density, impulse and energy (see Eq. (1)) (denoting $\vec{F} \cdot \vec{n}^0 = \{F_1, F_2, F_3\}$) can be represented as

$$F_1 = \begin{pmatrix} \rho(v_1\alpha_1 + v_2\beta_1 + v_3\gamma_1) \\ \rho v_1(v_1\alpha_1 + v_2\beta_1 + v_3\gamma_1) + p\alpha_1 \\ \rho v_2(v_1\alpha_1 + v_2\beta_1 + v_3\gamma_1) + p\beta_1 \\ \rho v_3(v_1\alpha_1 + v_2\beta_1 + v_3\gamma_1) + p\gamma_1 \\ (E + p)(v_1\alpha_1 + v_2\beta_1 + v_3\gamma_1) \end{pmatrix},$$

$$F_2 = \begin{pmatrix} \rho(v_1\alpha_2 + v_2\beta_2 + v_3\gamma_2) \\ \rho v_1(v_1\alpha_2 + v_2\beta_2 + v_3\gamma_2) + p\alpha_2 \\ \rho v_2(v_1\alpha_2 + v_2\beta_2 + v_3\gamma_2) + p\beta_2 \\ \rho v_3(v_1\alpha_2 + v_2\beta_2 + v_3\gamma_2) + p\gamma_2 \\ (E + p)(v_1\alpha_2 + v_2\beta_2 + v_3\gamma_2) \end{pmatrix},$$

$$F_3 = \begin{pmatrix} \rho(v_1\alpha_3 + v_2\beta_3 + v_3\gamma_3) \\ \rho v_1(v_1\alpha_3 + v_2\beta_3 + v_3\gamma_3) + p\alpha_3 \\ \rho v_2(v_1\alpha_3 + v_2\beta_3 + v_3\gamma_3) + p\beta_3 \\ \rho v_3(v_1\alpha_3 + v_2\beta_3 + v_3\gamma_3) + p\gamma_3 \\ (E + p)(v_1\alpha_3 + v_2\beta_3 + v_3\gamma_3) \end{pmatrix}. \tag{3}$$

Eqs. (1) and (3) are not completely divergent (conservative) because of the presence of constant vector H in Eq. (1). The reason for this is the noninertiality of the chosen coordinate system, which rotates with angular velocity ω. When the difference scheme based on equations system (1) is used, it is important to provide a precise application of the conservation laws of mass, energy and the axial (along z) component of the impulse caused by the uniformity of corresponding equations. Here the conservation law of the impulse for radial and angular components is not fully satisfied. If we use the difference approximation for other differential equations, the conservation law will not be satisfied.

The general computation algorithm is based on the principle of relaxation over time, i.e. it uses transition from a state in a moment in time equal to t_0 to a state at time $t_0 + \tau$.

The discretized form of Eq. (1) was obtained for this transition on an arbitrary moving grid according to Godunov et al. (1976); but this was extended to a more universal form for three space coordinates (Gnesin and Rządkowski, 2000).

Let the problem be characterized by the set of parameters at time t_0 in a grid of cells which cover the entire calculated domain. The flow parameters in the centre of each cell are given a fractional index $i + 1/2$, $j + 1/2$, $k + 1/2$:

$$\{p, \rho, v_1, v_2, v_3\}_{i+\frac{1}{2}, j+\frac{1}{2}, k+\frac{1}{2}}, \quad i = 1, \ldots M, \quad j = 1, \ldots N, \quad k = 1, \ldots L.$$

The parameters at time t are given a subscript index (i.e. $\rho_{i+1/2, j+1/2, k+1/2}$) as distinct from the parameters at the time $t_0 + \tau$, which are given a superscript (i.e. $\rho^{i+1/2, j+1/2, k+1/2}$). Here subscripts and superscripts correspond to the points of "old" and "new" grids, respectively.

A difference analogue of the conservation laws was obtained in the form used by Gnesin and Rządkowski (2002) by applying the integrals (1) to the moving grid cell (Fig. 1) with the number $(i + \frac{1}{2}, j + \frac{1}{2}, k + \frac{1}{2})$ during the time integral from t_0 to $t_0 + \tau$, and assuming that the velocity of points and gasodynamic parameters on the "middle" cell interface remain constant:

$$\frac{1}{\Delta t}\left[f^{i+\frac{1}{2}, j+\frac{1}{2}, k+\frac{1}{2}} \cdot \Omega^{i+\frac{1}{2}, j+\frac{1}{2}, k+\frac{1}{2}} - f_{i+\frac{1}{2}, j+\frac{1}{2}, k+\frac{1}{2}} \cdot \Omega_{i+\frac{1}{2}, j+\frac{1}{2}, k+\frac{1}{2}}\right]$$
$$+ \left[-(f\sigma w_n)_{i+1} + (f\sigma w_n)_i - (f\sigma w_n)_{j+1} + (f\sigma w_n)_j - (f\sigma w_n)_{k+1} + (f\sigma w_n)_k\right]$$
$$+ \left[(F_1\sigma)_{i+1} - (F_1\sigma)_i + (F_2\sigma)_{j+1} - (F_2\sigma)_j + (F_3\sigma)_{k+1} - (F_3\sigma)_k\right] + H_{i+\frac{1}{2}, j+\frac{1}{2}, k+\frac{1}{2}} \cdot \Omega_{i+\frac{1}{2}, j+\frac{1}{2}, k+\frac{1}{2}} = 0. \tag{4}$$
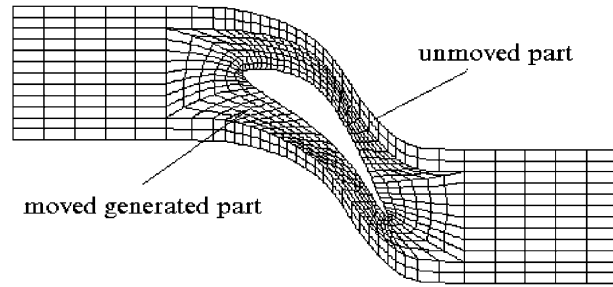
Fig. 1. Hybrid H–H (H–O)-type grid.

Here subscripts and superscripts correspond to "old" and "new" cells; f are "small" values in cell centres; F_1, F_2, F_3 are "big" values on the "middle" cell interface; σ and w_n are the area and normal velocity of the "middle" cell interface.

The following conditions at the discrete realization of the conservation laws (4) are assumed: (i) the "big" values calculated on the "old" cell interfaces transfer without change to the "middle" cell interface; (ii) the normal velocity w_n of the "middle" cell interfaces and the normal velocity of flow are defined as projections of vectors $\vec{w}$ and $\vec{v}$ on the normal to the "middle" cell interface.

The results of a steady calculation were used as the initial approximation of the unsteady problem. Because there is no strong proof of the correctness of this direct problem formulation, only experiment can serve as an acceptable criterion for the results of the numerical calculation.

On the blade surface, because the grid moves with the blade, the normal relative velocity is set to zero:

$$(\vec{v} - \vec{w}) \cdot \vec{n} = 0. \tag{5}$$

It is assumed that the unsteady flow fluctuations are due to prescribed blade motions, and the flows far upstream and far downstream from the blade row contain at most small perturbations of uniform free-streams. Therefore, the boundary conditions are based on the one-dimensional theory of characteristics, where the number of physical boundary conditions depends on the number of characteristics entering the computational domain.

In the general case, when the axial velocity is subsonic at the inlet boundary, initial values for total pressure, total temperature and flow angles are used in terms of a rotating frame of reference, while at the outlet boundary only static pressure has to be imposed. Reflecting boundary conditions can be used, i.e. incoming waves (three at the inlet and one at the outlet) have to be suppressed, which is accomplished by setting their time derivative equal to zero.

The total system of boundary conditions can be represented in the following form:

At inlet (Godunov et al., 1976, p. 323; Gnesin and Rządkowski, 2000):

$$T_0 = T_0(x, y), \quad p_0 = p_0(x, y), \quad \alpha = \alpha(x, y), \quad \gamma = \gamma(x, y), \quad d\left(v_3 - \frac{2a}{\lambda - 1}\right) = 0, \tag{6}$$

at outlet

$$p = p(x, y), \quad \mathrm{d}p - a^2\,\mathrm{d}p = 0, \quad \mathrm{d}v_1 - \left(\omega^2 r - 2\omega v_2\right)\mathrm{d}t = 0, \quad \mathrm{d}v_2 + 2\omega v_1\,\mathrm{d}t = 0, \quad d\left(v_3 + \frac{2a}{\lambda - 1}\right) = 0, \tag{7}$$

where $a = \sqrt{\lambda(p/\rho)}$ is the sound velocity.

On the blade surface, zero flux is applied across the solid surface (the grid moves with the blade).

3. Structural model

The structural model is based on a linear model, the mode shapes and natural frequencies being obtained via standard finite element (FE) analysis techniques. The mode shapes are interpolated from the structure mesh onto the aerodynamic mesh.

The structural part of the aerodynamic equations of motion is uncoupled by using the mode shape matrix and the modal superposition method.

The first step of the modal approach consists of solving the problem of the natural mode shapes and eigenvalues. Then, the displacement of each blade can be written as a linear combination of the first N mode shapes with the modal

coefficients depending on time:

$$\bar{u}(x,t) = \bar{U}(x,t)q(t) = \sum_{i=1}^{N} \bar{U}_i(x)q_i(t), \tag{8}$$

where $U_i(x)$ is the displacement vector corresponding to ith mode shape, and $q_i(t)$ is the modal coefficient of ith mode.

Functions U satisfy the orthogonal conditions and the normalization condition (Rządkowski, 1998, 2004), so the equation of motion is reduced to a set of independent differential equations, relatively to modal coefficients of the mode shapes:

$$\ddot{q}_i(t) + \omega_i^2 q_i(t) = \lambda_i(t), \quad i = 1, \ldots, N, \tag{9}$$

where $\omega_i = 2\pi f_i$, f_i is the ith natural frequency in Hz.

The modal forces λ_i are calculated at each iteration [see Rządkowski (1998, p. 95) and Gnesin and Rządkowski (2000)] with the use of the instantaneous pressure field calculated for all cells of the blade in the following way:

$$\lambda_i = \frac{\int\int_\sigma p \bar{U}_i \cdot \bar{n}^\circ \, d\sigma}{\int\int\int_v \rho \bar{U}_i^2 \, dv}. \tag{10}$$

Here the numerator represents the work of pressure forces at the blade displacement in accordance with the ith mode; the denominator represents the normalizing factor. Having defined the modal coefficients from equation set (9), blade displacement and velocity can be obtained in the form of (8).

Boundary conditions from the structural and aerodynamic domains are exchanged at each step and the aeroelastic mesh is moved to follow the structural motion.

The numerical calculations were performed to compare the theoretical results with experiments presented by Bolcs and Fransson (1986). The calculations were carried out for the torsional oscillations of a compressor cascade known as the First Standard Configuration (Bolcs and Fransson, 1986) and for the bending oscillations of a turbine cascade known as the Fourth Standard Configuration (Bolcs and Fransson, 1986). The comparison of calculated and experimental results of the 1st and 4th Standard Configurations has shown good quantitative and qualitative agreement for both integral performances (aerodamping coefficient) and local performances (unsteady pressure amplitude and phase distribution) (Rządkowski and Gnesin, 2000; Gnesin and Rządkowski 2002).

4. Numerical results

Numerical calculations were carried out for the rotor turbine blades. The important properties of the blade disc are as given below: the disk inner radius $r_0 = 0.27$ m, the bladed-disk junction radius $R = 0.667$ m and the blade length $L = 0.765$ m. All geometrical parameters of the blade are presented by Rządkowski (1998).

Numerical calculations were performed for harmonic oscillations of the blade row according to natural modes with the same amplitude and IBPA. The first mode was mainly one of bending, the second one was both of bending and of torsion, the third one concerned torsion, whereas the fourth and fifth modes combined bending and torsion. The natural frequencies of a non-rotating blade were equal to 41.3, 99.1, 216.3, 220.8 and 320.6 Hz, respectively.

The aeroelastic behaviour of the vibrating blade row is defined by the aerodamping coefficient D which is equal to the negative work coefficient performed during one cycle of oscillations.

Figs. 2–6 show the aerodamping coefficient (averaged over the blade length) versus the IBPA for the 1st, 2nd, 3rd, 4th and 5th natural mode shapes respectively for harmonic oscillations with different natural frequencies f_i. The calculations were done using Eq. (9) for different natural frequencies f_i, assuming that the ith mode shape is unchanged. The negative values of D correspond to the transfer of the mean flow energy to the blade (self-excitation), and positive values to the dissipation of oscillating blade energy to the flow (aerodamping).

All the curves have typical sinusoidal forms. It is apparent that the aerodamping value grows as the oscillation frequency increases.

It should be pointed out that according to the first mode (bending oscillations) the oscillations are characterized by minimal values of an aerodamping coefficient near the $-90°$ IBPA (see Fig. 2) and the transfer of the flow energy to the blade ($D < 0$, flutter condition) for natural frequencies $f < 50$ Hz. The oscillations according to the third mode (torsional oscillations) have the self-excitation area near the $90°$ IBPA and for natural frequencies $f < 300$ Hz (see Fig. 4).

The oscillations according to the 2nd mode, in which both bending and torsional motions occur, are damped for all vibration frequencies and have minimal values of an aerodamping coefficient near the $0°$ IBPA.
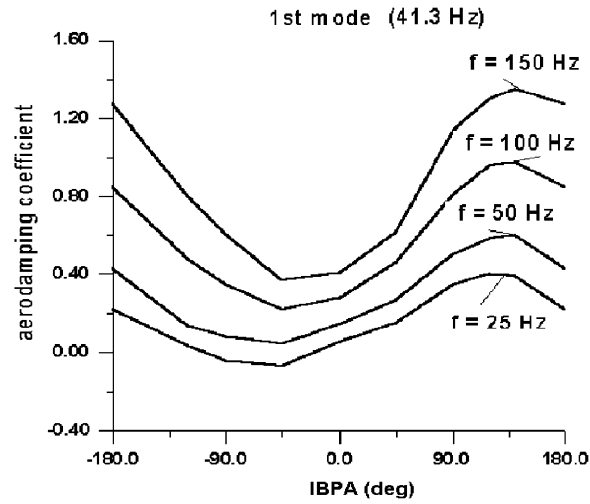
Fig. 2. Aerodamping coefficient versus IBPA for the 1st mode and different natural frequencies.
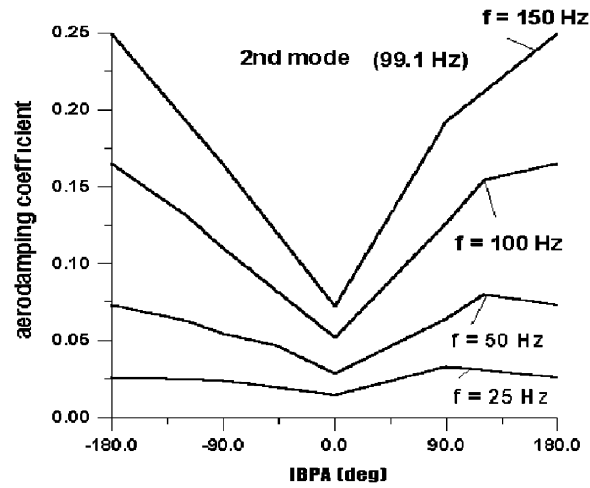

Fig. 3. Aerodamping coefficient versus IBPA for the 2nd mode and different natural frequencies.
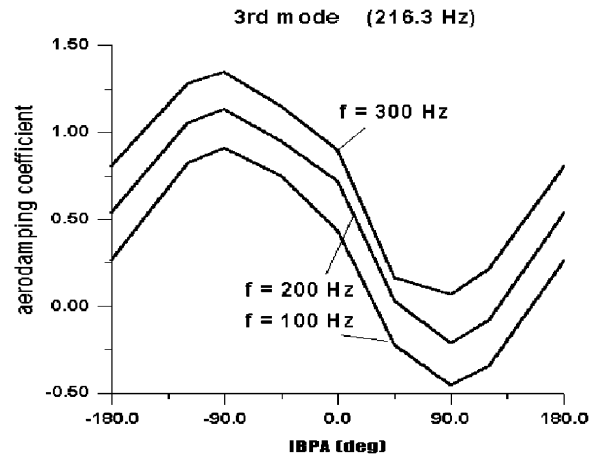

Fig. 4. Aerodamping coefficient versus IBPA for the 3rd mode and different natural frequencies.
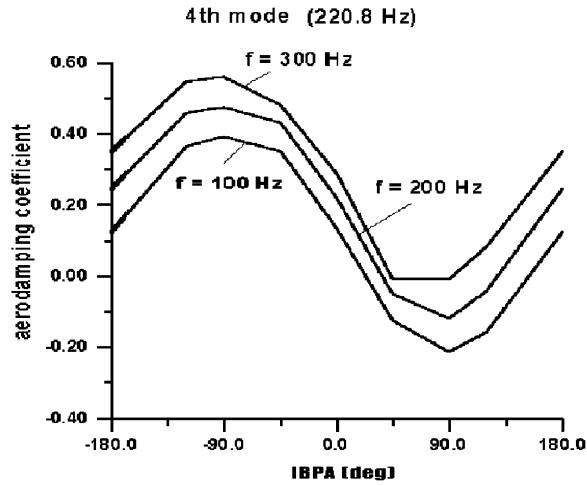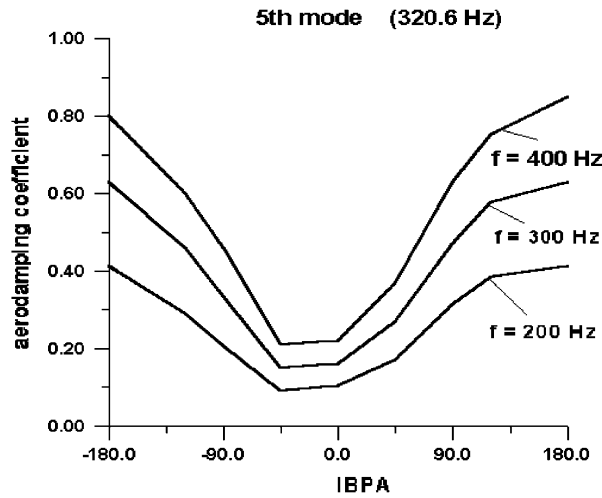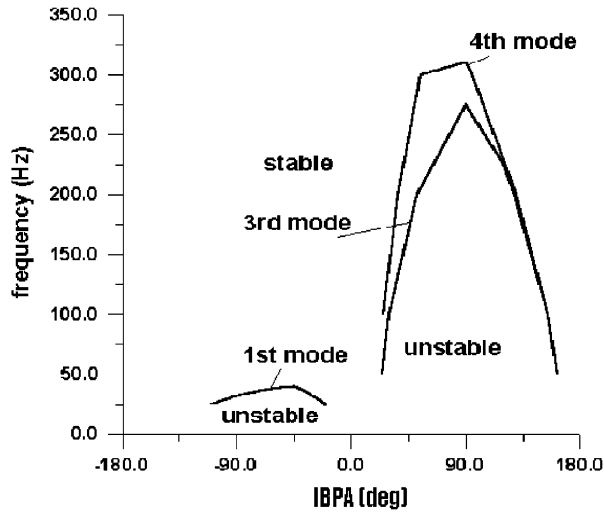
4th mode (220.8 Hz)

Fig. 5. Aerodamping coefficient versus IBPA for the 4th mode and different natural frequencies.

5th mode   (320.6 Hz)

Fig. 6. Aerodamping coefficient versus IBPA for the 5th mode and different vibration frequencies.

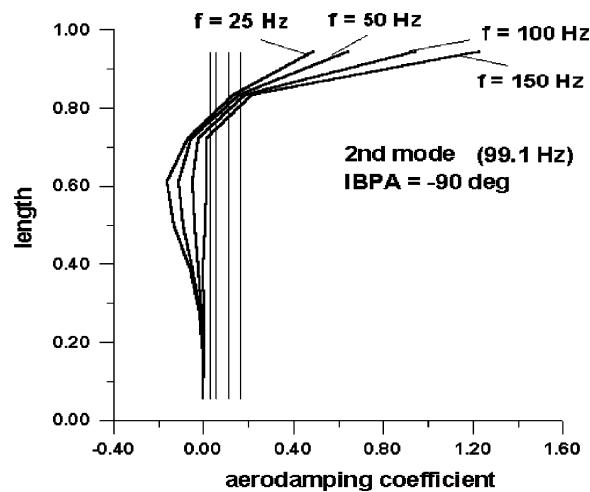Fig. 7. The stability (instability) areas for the first four natural mode shapes.
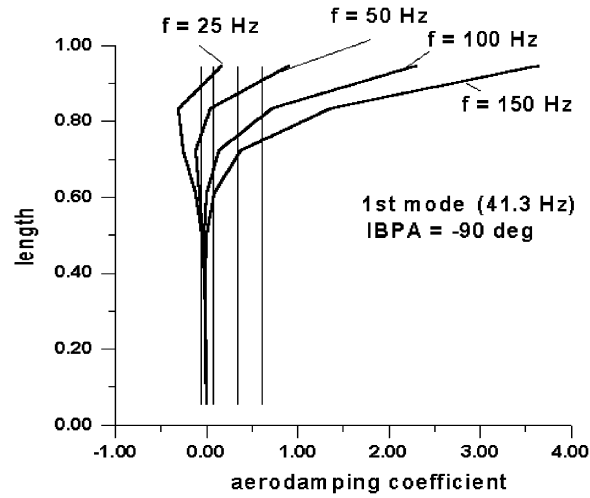
Fig. 8. The aerodamping coefficient distribution over the blade length for the 1st mode, IBPA = −90°.
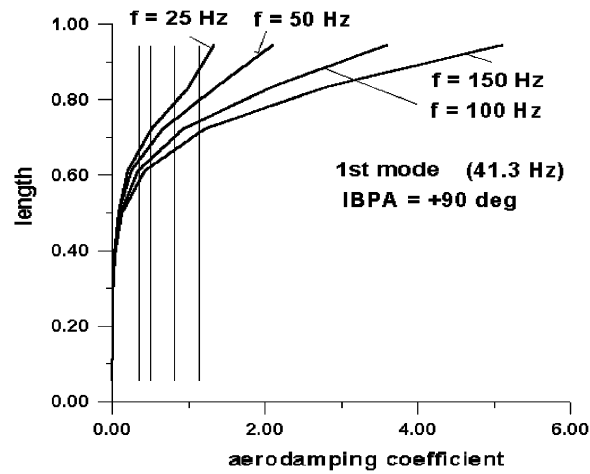
Fig. 9. The aerodamping coefficient distribution over the blade length for the 1st mode, IBPA = 90°.

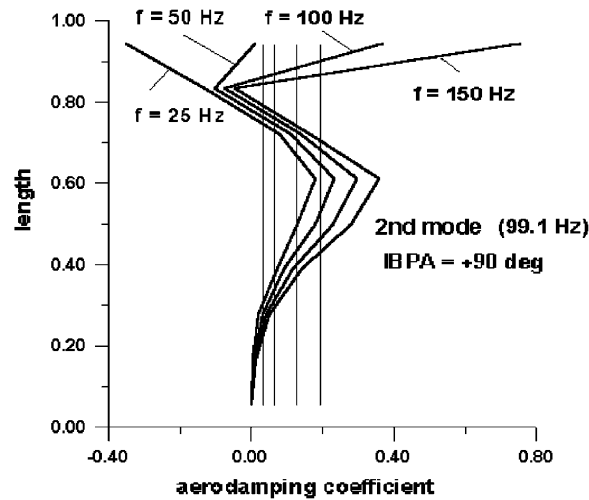Fig. 10. The aerodamping coefficient distribution over the blade length for the 2nd mode, IBPA = −90°.

Fig. 11. The aerodamping coefficient distribution over the blade length for the 2nd mode, IBPA = 90°.
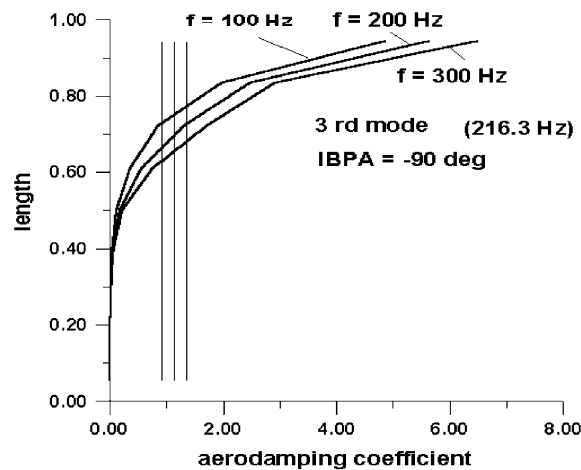

Fig. 12. The aerodamping coefficient distribution over the blade length for the 3rd mode, IBPA = −90°.

The shape of the aerodamping coefficient versus the IBPA for 4th mode is similar to the 3rd mode (see Figs. 4 and 5). The level of the aerodamping coefficient is lower, but the area of negative values of the aerodamping coefficient appears for a natural frequency $f < 300$ Hz.

Fig. 7 shows the areas of possible instability for the long blade. It can be seen that instability of the first mode appears near the −90° IBPA and with frequencies lower than 50 Hz. The instability of the 3rd and 4th modes occurs at the IBPA values $30° \leqslant \delta \leqslant 150°$ and with vibration frequencies lower than 350 Hz. Oscillations in the 2nd and 5th modes are stable over the full frequency range.

Figs. 8–17 present aerodamping coefficients along the entire blade length for a wide range of natural frequencies and for each of the five mode shapes in turn with the IBPA being equal to −90° and +90°.

In these figures the averaged aerodamping coefficients for the considered mode shape and natural frequencies are shown as vertical lines.

In the case of the 1st mode shape (see Fig. 8) with a natural frequency $f = 25$ Hz and the IBPA −90° the flutter appears in the region of 0.6–0.9 of the blade length. When $f = 50$ Hz the flutter appears in the region of 0.6–0.8 of the blade length. There is no flutter for the frequencies of 100 and 150 Hz. Likewise, when the IBPA is equal to 90° (see Fig. 9) there is no flutter.
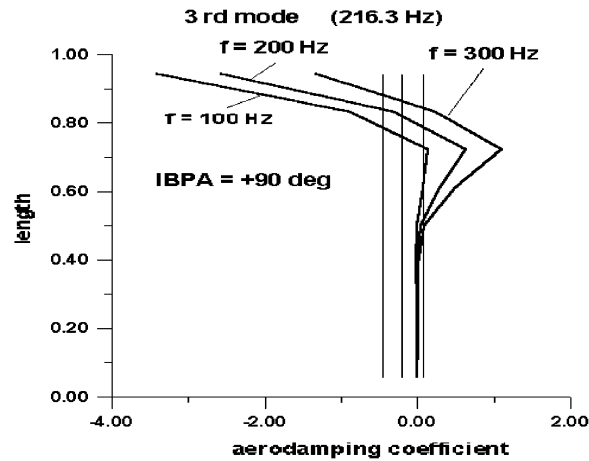
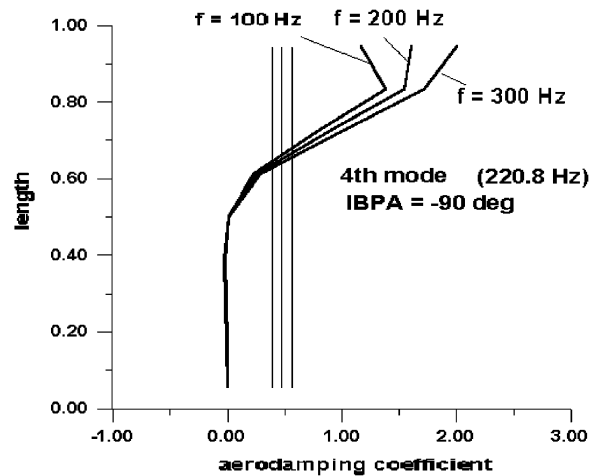Fig. 13. The aerodamping coefficient distribution over the blade length for the 3rd mode, IBPA = 90°.

Fig. 14. The aerodamping coefficient distribution over the blade length for the 4th mode, IBPA = −90°.

For the 2nd mode shape (Fig. 11) with a natural frequency of 25 Hz and the IBPA of 90° the flutter appears in the region of 0.71–1.0 of the blade length. When $f = 50$ Hz it appears in the region of 0.72–1.0; $f = 100$ Hz in the region of 0.73–0.95 and when $f = 150$ Hz in the region of 0.74–0.91 of the blade. The average aerodynamic coefficient along the blade length for all these frequencies is positive. When the IBPA equals −90° (Fig. 10), the aerodamping coefficient is positive for all frequencies.

Analyzing the 3rd mode shape (see Fig. 13) with a natural frequency of 100 Hz and the IBPA of 90° the flutter appears in the region of 0.74–1.0 of the blade length; with $f = 200$ Hz in the region of 0.81–1.0 and with $f = 300$ Hz in the region of 0.85–1.0. The average aerodynamic coefficient along the blade length is negative for frequencies of 100 and 200 Hz and positive for 300 Hz. Flutter is not observed for an IBPA equal to −90° (see Fig. 12).

In the case of 4th mode shape (see Fig. 15) with a natural frequency of 100 Hz and the IBPA of 90° the flutter appears in the region of 0.61–0.95 of the blade length; for $f = 200$ Hz in the region of 0.63–0.94; $f = 300$ Hz in the region of 0.70–0.83. The average aerodynamic coefficient along the blade length for these frequencies is negative. Flutter is not seen when the IBPA is equal to −90° (Fig. 14).

For the 5th mode shape (see Fig. 16) with natural frequencies of 200 and 300 Hz flutter appears in the region of 0.7–0.85 of the blade length, whereas when $f = 400$ Hz flutter does not appear. The average aerodynamic coefficient along the blade length for these frequencies is positive. For an IBPA equal to +90° (see Fig. 17) the aerodynamic coefficient changes along the blade length and is positive.
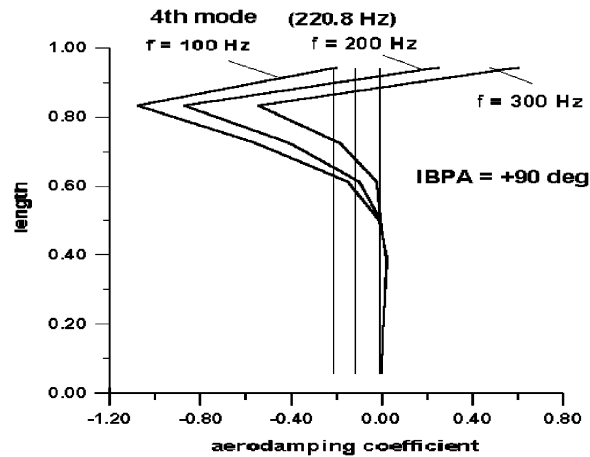
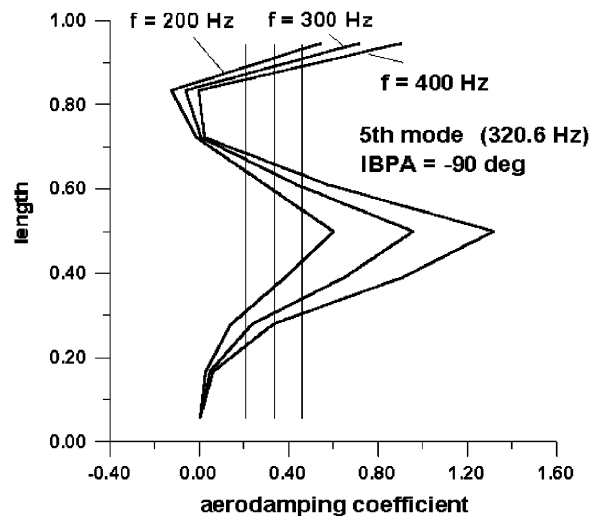Fig. 15. The aerodamping coefficient distribution over the blade length for the 4th mode, IBPA = 90°.

Fig. 16. The aerodamping coefficient distribution over the blade length for the 5th mode, IBPA = −90°.

It is interesting to note that the sign of the aerodamping coefficient changes along the blade length. On a part of the blade the aerodamping coefficient is negative $D < 0$ (the flutter condition), while on another part of the blade the aerodamping coefficient is positive $D > 0$ (the damping condition). These areas change depending on the mode shape.

Presented next in this paper are the numerical results of coupled oscillations for each of the natural modes (Eq. (9)). Here the IBPA values correspond to the minimal values of the aerodamping coefficient. Fig. 18 presents the aeroelastic response of the blade row vibrating in the 1st mode with a natural frequency of 50 Hz and an IBPA of −90°. Fig. 8 shows the aerodamping coefficient distribution over the blade length for harmonic oscillations. When $f = 50$ Hz, the transfer of energy from the flow to the blade (flutter condition) appears from the root to 4/5 of the blade length and the dissipation of blade energy starts from 4/5 of the blade length to the blade tip. The averaged aerodamping coefficient over the blade length takes a positive value ($D = 0.02$), which corresponds to the stability of the blade oscillation.

All calculations are run from the very beginning for harmonic oscillations (in accordance with particular mode shapes). At a point in time, named "the started regime", coupled vibrations (the coupled fluid–structure interaction Eq. (8)) begin. Fig. 18 illustrates the two adjacent blade responses. The harmonic oscillation continues throughout one period and then the coupled vibrations begin. The amplitude of oscillations of the 1st mode decays.
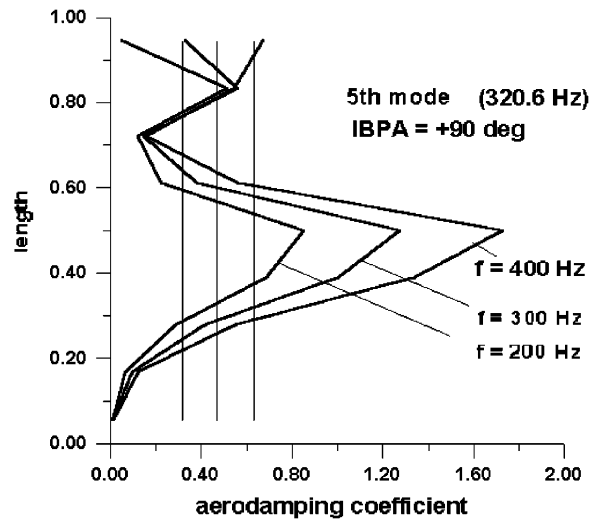
Fig. 17. The aerodamping coefficient distribution over the blade length for the 5th mode, IBPA = 90°.
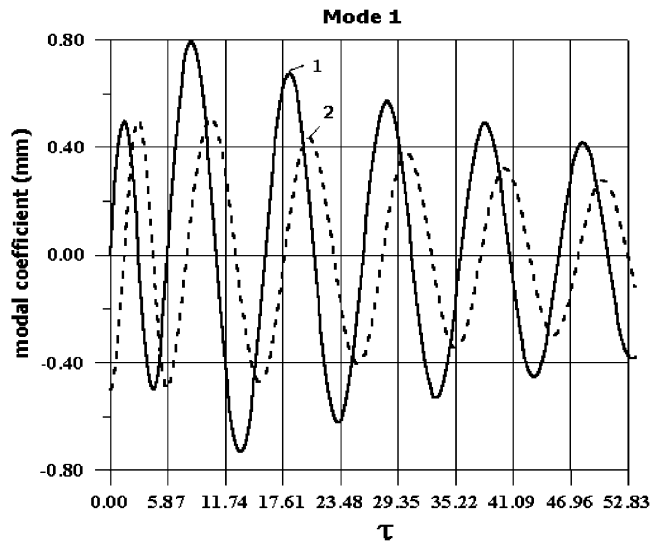

Fig. 18. Coupled oscillations in the 1st mode for two adjacent blades, IBPA = −90°, δ = 0.155, $t = \tau/316$ s.

The logarithmic decrement (log dec) is defined as

$$\delta = \frac{1}{n} \ln \frac{A_1}{A_n},$$

where n is the number of cycles; A_1 and A_n are amplitudes of the first cycle and the nth cycle, respectively. In this case the logarithmic decrement is equal to δ = 0.155.

The work coefficient for each of the blades (four passages in this case) is shown in Fig. 19. The monotonic convergence of the work coefficient to zero demonstrates the dissipation of the vibrating blades energy into the flow field.

Next to be calculated is the aeroelastic response of blade row vibrating in the 2nd mode with the natural frequency of 100 Hz and IBPA equal to 0°.
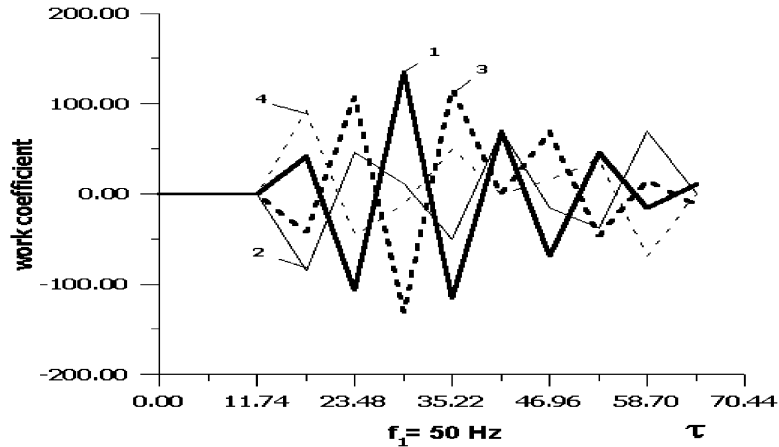
Fig. 19. The work coefficient change at the coupled oscillations in the 1st mode, IBPA $= -90°$, $t = \tau/316$ s.
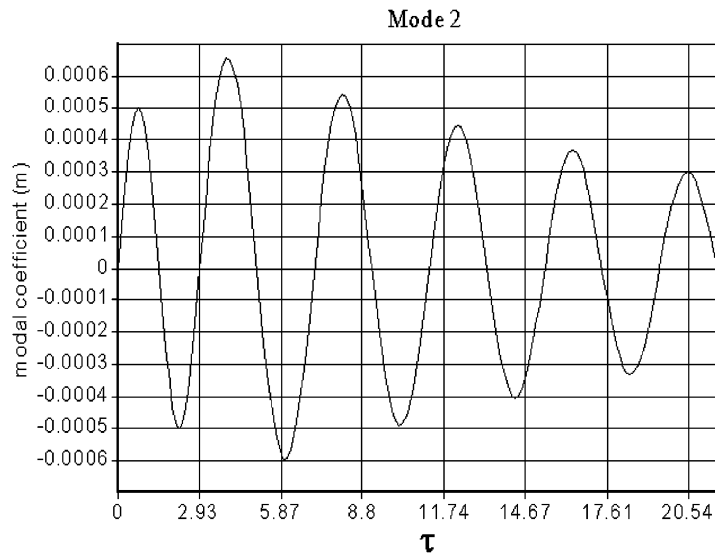

Fig. 20. Coupled oscillations in the 2nd mode and IBPA $= 0°$, $\delta = 0.195$, $t = \tau/316$ s.

The aerodamping coefficient distribution over the blade length for harmonic oscillations is similar to the case of harmonic oscillations with the frequency of 100 Hz and an IBPA equal to $-90°$ (see Fig. 10). The averaged aerodamping coefficient for harmonic oscillations in the 2nd mode is positive and equal to 0.09.

The modal coefficient change versus the time for the coupled fluid–structure vibrations in the 2nd mode is presented in Fig. 20. The first cycle corresponds to the harmonic oscillations, the others to the coupled oscillations. The coupled vibrations decay. The logarithmic decrement for this mode of vibration is equal to $\delta = 0.195$.

The next calculation concerns the aeroelastic response of blade row vibrating in the 3rd mode with the frequency of 200 Hz and the IBPA equal to 90°. The averaged aerodamping coefficient for harmonic oscillations in the 3rd mode is negative and equal to -0.25 (see Fig. 13). The modal coefficient versus the time for the coupled fluid–structure vibrations in the 3rd mode is presented in Fig. 21. The first cycle corresponds to harmonic oscillations, while the others correspond to coupled oscillations. In this case the coupled vibrations decay. The logarithmic decrement of this mode is equal to $\delta = 0.2$.

Even though the flutter conditions appear in the harmonic oscillations, the blade response in the coupled vibration decreases. This fact can be explained in the following way: the value and sign of the nondimensional aerodamping coefficient for the harmonic oscillations depends only on the nondimensional aerodynamic parameters of a given flow
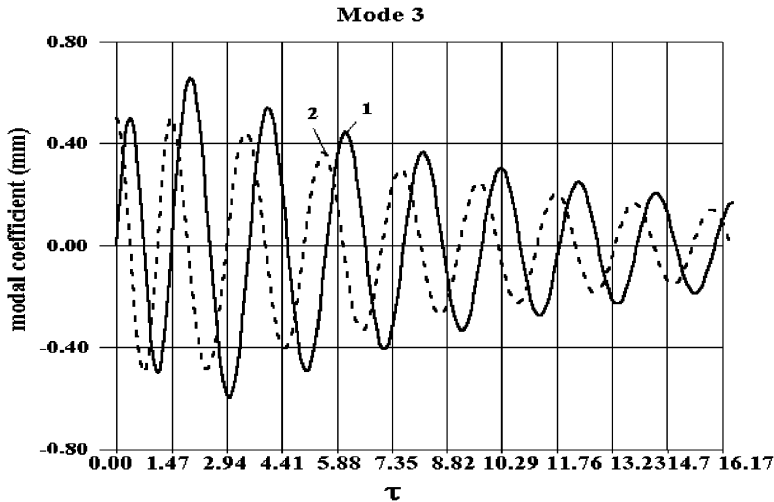
Fig. 21. Coupled oscillations in the 3rd mode, IBPA $+90°$, $\delta = 0.2$.

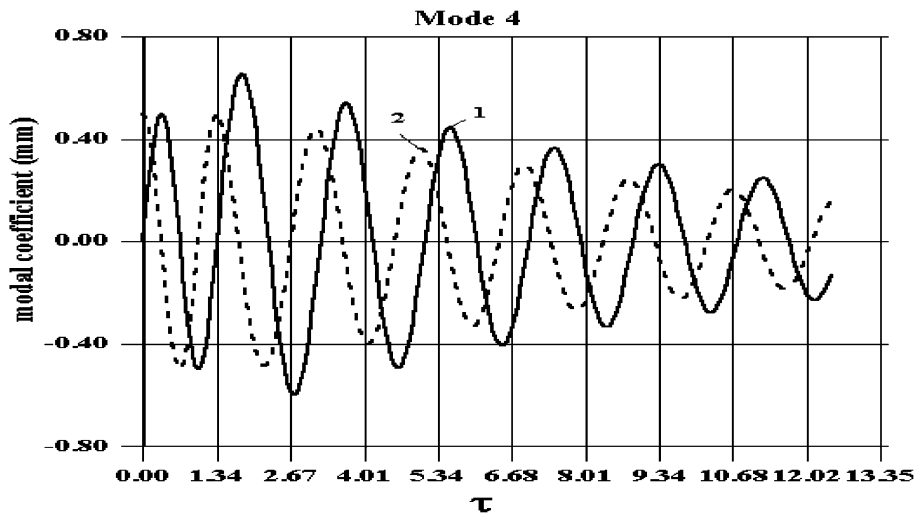Fig. 22. Coupled oscillations in the 4th mode, IBPA $= +90°$, $\delta = 0.195$, $t = \tau/316$ s.

field and the blade oscillations mode. Therefore, the aerodamping coefficient characterizes the energy exchange between the flow and the blade. The sign of the aerodynamic coefficient may be considered as a necessary but not sufficient condition for self-excited vibrations. The blade response depends on the energy value transfer from the flow to the blade, and on the blade kinetic energy of coupled fluid–structure oscillations. If the values of transferring energy are much less than the blade kinetic energy of the coupled vibrations, the blade oscillations are damped after the kinematic excitation is removed.

Fig. 22 presents the aeroelastic response of the blade row vibrating in the 4th mode with the frequency of 220 Hz and the IBPA equal to 90°. The averaged aerodamping coefficient is equal to −0.1 (see Fig. 15). As in the previous case (3rd mode) the aerodamping coefficient in the harmonic vibration takes a negative value that corresponds to the flutter condition, but in the coupled oscillations the blade response is damped (see Fig. 22) with the logarithmic decrement equal to 0.195.

Fig. 23 presents the aeroelastic response of the blade row vibrating in the 5th mode with an excitation frequency of 320 Hz and the IBPA equal to −45°.

It should be noted that in each of the modes considered above, the coupled damping oscillations are realised with approximately the same logarithmic decrement ($\delta \approx 0.195$) but with different frequencies. Generally, the frequency of
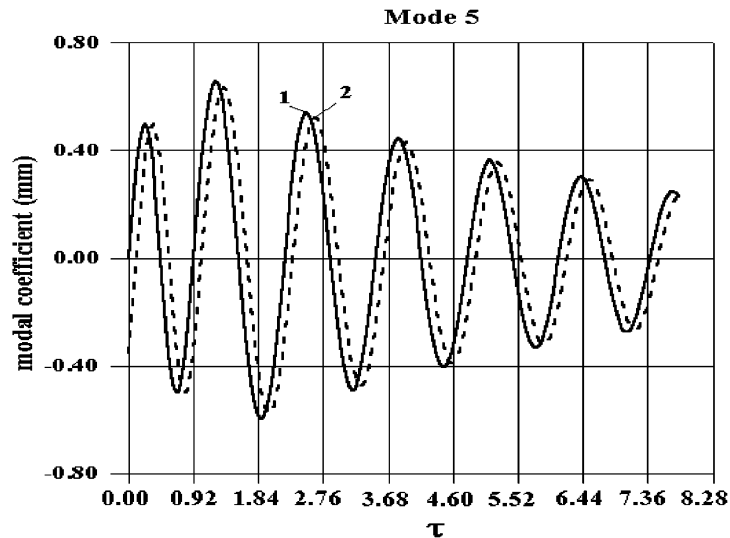
Fig. 23. Blade displacements at coupled oscillations in the 5th mode, IBPA $= -45°$, $t = \tau/316$ s.

the coupled vibrations decreases by 30% in relation to the value of the natural frequencies (see Figs. 18 and 20–23). So, the damping time is inversely proportional to the excitation frequency of the oscillations.

5. Conclusions

In the study presented the simultaneous time domain method and the modal superposition method have been used to determine the aeroelastic stability of the cascade. The influence of the natural modes on the aeroelastic blade response for long steam turbine blades was analysed numerically.

Numerical calculations were performed for harmonic oscillations of the blade row in various natural modes with the same amplitude and interblade phase angle (IBPA).

The time domain method presented allows for a more realistic simulation of the interaction between the flow and vibrating blades, which should lead to a better physical understanding of flutter.

This paper has also demonstrated the influence of both the IBPA and the natural frequency on the aerodamping value.

Moreover, progress has been made in better understanding the aerodamping coefficient for the mode shapes considered along the blade length. It is interesting to see that the aerodamping coefficient sign changes along the blade length and is dependant on the mode shape. In a part of the blade it is negative, while in another part of the blade it is positive. These areas change depending on the mode shape.

The blade responses for all coupled oscillation regimes considered are damped.

References

Bakhle, M.A., Reddy, T.S.R., Keith, T.G., 1992. Time domain flutter analysis of cascades using a full−potential solver. AIAA Journal 30, 163.

Bendiksen, O.O., 1998. Nonlinear blade vibration and flutter in transonic rotors. In: Proceedings of ISROMAC—7, Seventh International Symposium on Transport Phenomena and Dynamics of Rotating Machinery, February 22−26, 1998. Honolulu, Hawaii, USA, p. 664.

Bolcs A., Fransson, T.H., 1986. Aeroelasticity in Turbomachines: Comparison of Theoretical and Experimental Cascade Results, Communication du LTAT−EPFL Switzerland, No. 13, p. 174.

Carstens, V., Belz, J., 2000. Numerical Investigation of Nonlinear Fluid–Structure Interaction in Vibrating Compressor Blades. ASME paper 2000-GT-0381.

Gnesin, V.I., Kolodyazhnaya, L.V., 1999. Numerical modelling of aeroelastic behaviour for oscillating turbine blade row in 3D transonic ideal flow. Problems in Machinery Engineering 1, 65−76.

Gnesin, V., Kolodyazhnaya, L., Rządkowski, R, 2001. Coupled aeroelastic oscillations of a turbine blade row in 3D transonic flow. Journal of Thermal Science 10, 318–324.

Gnesin, V., Rządkowski, R., 2000. The theoretical model of 3D flutter in subsonic, transonic and supersonic inviscid flow. Transactions of the Institute of Fluid-Flow Machinery 106, 45–68.

Gnesin, V., Rządkowski, R., 2002. A coupled fluid–structure analysis for 3D inviscid flutter of IV standard configuration. Journal of Sound and Vibration 251, 315–327.

Gnesin, V., I., Rzadkowski, R., Kolodyazhnaya, L.V., 2000. A coupled Fluid–Structure Analysis for 3D Flutter in Turbomachines. ASME paper 2000-GT-0380.

Godunov, S.K., Zabrodin, A.V., Ivanov, M.Y., Krajko, A.N., Prokopov, G.P., 1976. Numerical Solution of Multidimensional Problems in Gasdynamics. Nauka, Moscow (in Russian).

He, L., 1984. Integration of 2D fluid/structure coupled systems for calculation of turbomachinery aerodynamic, aeroelastic instabilities. Journal of Computational Fluid Dynamics 3, 217–227.

He, L., Ning, W., 1998. Nonlinear harmonic analysis of unsteady transonic inviscid and viscous flows. Unsteady aerodynamics and aeroelasticity of turbomachines. In: Proceedings of the Eighth International Symposium held in Stockholm, Sweden, September 14–18, pp. 183–189.

Marshall, J.G., Imregun, M., 1996. A review of aeroelasticity methods with emphasis on turbomachinery applications. Journal of Fluids and Structures 10, 237–257.

Moyroud, F., Jacquet-Richardet, G., Fransson, T.H., 1996. A Modal Coupling for Fluid and Structure Analysis of turbomachines Flutter Application to a Fan Stage, ASME Paper 96-GT-335.

Rządkowki, R., 2004. Flutter of Turbine Rotor Blades in Inviscid Flow, Wydawnictwo Akademii Marynarki Wojennej, Gdynia.

Rządkowski, R., 1998. Dynamics of Steam Turbine Blading, Part 2: Bladed Discs. Ossolineum, Wrocław-Warszawa.

Rządkowski, R., Gnesin, V., 2000. The numerical and experimental verification of the 3D inviscid code. Transactions of the Institute of Fluid-Flow Machinery 106, 69–95.

Rządkowski, R., Gnesin, V., Kovalov, A., 1998. The 2D flutter of bladed disc in an incompressible flow. Unsteady aerodynamics and aeroelasticity of turbomachines. In: Proceedings of the Eighth International Symposium held in Stockholm, Sweden, September 14–18, pp. 317–334.